

**Peter H. Wilkins<sup>1</sup>**

Department of Mechanical Engineering,  
Pennsylvania State University,  
University Park, PA 16802  
e-mail: phw13@psu.edu

**Stephen P. Lynch**

Department of Mechanical Engineering,  
Pennsylvania State University,  
University Park, PA 16802  
e-mail: splynch@psu.edu

**Karen A. Thole**

Department of Mechanical Engineering,  
Pennsylvania State University,  
University Park, PA 16802  
e-mail: kthole@psu.edu

**San Quach**

Pratt & Whitney, a Division of Raytheon  
Technologies Corporation,  
East Hartford, CT 06118  
e-mail: san.quach@prattwhitney.com

**Tyler Vincent**

Pratt & Whitney, a Division of Raytheon  
Technologies Corporation,  
East Hartford, CT 06118  
e-mail: tyler.vincent2@prattwhitney.com

# Experimental Heat Transfer and Boundary Layer Measurements on a Ceramic Matrix Composite Surface

*Ceramic matrix composites (CMCs) are quickly becoming more prevalent in the design of gas turbines due to their advantageous weight and thermal properties. While there are many advantages, the CMC surface morphology differs from that of conventional cast airfoil components. Despite a great deal of research focused on the material properties of CMCs, little public work has been done to investigate the impact that the CMC surface morphology has on the boundary layer development and resulting heat transfer. In this study, a scaled-up CMC weave pattern was developed and tested in a low-speed wind tunnel to evaluate both heat transfer and boundary layer characteristics. Results from these experiments indicate that the CMC weave pattern results in augmented heat transfer and flow field properties that significantly vary locally when compared with a smooth surface. [DOI: 10.1115/1.4050314]*

**Keywords:** boundary layer development, heat transfer and film cooling, measurement techniques, ceramic matrix composites

## Introduction

Ceramic matrix composites (CMCs) have been an appealing option for gas turbine designers due to favorable thermal and weight properties at high temperatures, creating the potential for lighter and more efficient gas turbines than the metal alloys that are currently used [1]. In addition to having exceptional weight and thermal properties, CMCs have good oxidation resistance at high temperatures [2]. The increase in allowable component temperature limits for CMCs allows for gas turbines to operate at higher turbine entry temperatures with reduced cooling requirements that improve turbine efficiencies. Another major advantage of CMCs over their metallic counterparts is their relatively low density, contributing to a lighter turbine and improving the thrust-to-weight ratio [3].

Some challenges for CMCs relative to conventional turbine superalloys are their susceptibility to brittle fracture, thermal shock sensitivity, potential degradation due to water vapor in the combustion products, and inherent surface roughness. The focus over the past few decades has been on improving the strength, durability, and manufacturability of CMCs, which has led to recent implementations in military and commercial aircraft engines. While there has been substantial progress in the improvement of mechanical properties, there has been little work investigating how the surface morphology of CMCs can influence the boundary layer development over a turbine component. The weave pattern of a typical CMC surface creates a multi-scale roughness profile that consists of large features related to the weave, moderate scale roughness associated with fibers and small-scale roughness due to surface treatment or the manufacturing process. In question is

whether a designer can use the direction of a particular weave pattern to get a desirable heat transfer distribution.

This study is unique because it examines how the large-scale roughness of the weave pattern of a CMC material can impact the local heat transfer coefficient and boundary layer formation over a range of Reynolds numbers relevant to the high-pressure turbine operation. Spatially resolved heat transfer coefficients and detailed flow field measurements are obtained on the surface and compared with smooth surfaces.

## Background

Over the past few decades, the majority of the research on CMCs has targeted the improvement of their mechanical properties, such as reducing negative effects from oxidation and slowing crack growth at elevated temperatures while pushing ever higher temperatures [4–6]. These studies have improved the mechanical properties to the point where rotating components are starting to show promise and static components have been integrated into commercial engines [3,7,8]. However, CMCs have atypical surface features relative to conventional gas turbine materials, and little work has investigated how this might impact the boundary layer development and local heat transfer.

The effect of surface roughness on heat transfer coefficients over gas turbine components has been a topic of substantial research. Bogard et al. [9] measured roughness of real turbine surfaces ( $R_a$ ) and converted it into an equivalent sand grain roughness height  $k_s$ . An analog surface with the same  $k_s$  was generated in a constant heat flux foil to calculate St augmentation. From this analysis, Bogard et al. determined that using  $R_a$  values to create roughness profiles equivalent to measured “true” rough surfaces was inadequate for predicting heat transfer and flow performance. An extensive literature survey by Bons [10] found that while current approaches for representing surface roughness in turbomachinery components are able to define general trends, accurately predicting

<sup>1</sup>Corresponding author.

Contributed by the International Gas Turbine Institute (IGTI) of ASME for publication in the JOURNAL OF TURBOMACHINERY. Manuscript received November 29, 2020; final manuscript received February 19, 2021; published online April 8, 2021. Tech. Editor: David G. Bogard.

the flow and heat transfer properties for a given surface is still beyond present capabilities. The use of  $k_s$  to represent surface roughness does not capture the richness of the surface morphology in a sufficiently generalizable way. It is important to note that both of these reported studies were for random roughness, whereas CMCs produce a combination of random plus periodic protrusions. Another study by Bons and McClain [11] reinforced this idea where they investigated the effects of real roughness and saw that even in an area-averaged sense matched roughness statistics did not accurately represent the heat transfer or boundary layer behavior. The unique surface features created by the weave patterns of a CMC result in a surface that probably also cannot easily be characterized by existing roughness correlations.

Wavy surfaces, while not identical to the surface of a CMC, serve as a reference point to understand the surface morphology effects of a CMC. Buckles et al. [12] measured the boundary layer over a sinusoidal surface with a wavelength-to-amplitude ratio of  $\lambda/A = 10$ . They discovered a large separated region in the trough of the sinusoid and the fluctuations in the streamwise velocity in and around this separated region. Mamori et al. [13] computed the flow fields using direct numerical simulation (DNS) for a variety of wavelength-to-amplitude ratios for sinusoidal surfaces. From these simulations, Mamori et al. found that for larger wavelength-to-amplitude ratios of  $\lambda/2A = 12.5$ , the separation region is dominated by reverse flow. In another numerical study by Busse et al. [14], a graphite and grit blasted channel surface had substantial recirculation zones directly behind protruding features, which decreased in magnitude with increasing  $Re$ .

Of the few studies that have investigated CMC heat transfer, some have focused on cooling technologies enabled by CMCs. Taking advantage of the potential to incorporate porosity into a CMC, Prokein et al. [15] investigated the transpiration cooling effect of a porous CMC surface. Additionally, Zhong and Brown [16] investigated cooling effectiveness of various CMC combustor liners, finding that oxide-oxide CMCs have a reduction in cooling effectiveness as  $Re_x$  increases due to their relatively low thermal conductivity. While both explored how cooling can be integrated into a CMC, neither looked specifically at how the surface of a CMC changes the external flow characteristics.

To the authors' knowledge, there are only two prior studies that have investigated the effect of a unique surface topography of a CMC on heat transfer coefficients. Krishna et al. [17] investigated the augmentation in the Nusselt number from an impinging jet over a CMC surface using a three-dimensional (3D)-printed analog at real scale. From this analysis, it was found that the transition from laminar to turbulent flow occurred earlier than for a smooth plate and the orientation of the CMC had an effect on the Nusselt number at a given location. Building upon this research, Krishna and Ricklick [18] found using a machined surface that more closely matched CMC surface scans resulted in a significantly lower Nusselt augmentation than in the previous study [17]. The Nusselt augmentation in Krishna and Ricklick [18] was so much lower the authors determined that the augmentation seen in the previous study was more likely due to the roughness created by the finite steps present in the 3D printing process.

The public literature lacks detailed data associated with the heat transfer and boundary layer characteristics resulting from weave patterns relevant to CMCs for turbine applications. This makes it challenging to design adequate cooling systems for CMCs since their augmentation relative to conventional turbine materials is unknown. The uniqueness of this particular study is that it fills a void in this knowledge, through spatially resolved measurements of surface heat transfer coefficients and detailed boundary layer measurements.

## Description of Ceramic Matrix Composite Surface

A geometric model that represents the distinct weave pattern of a CMC was developed for this work. A mathematically defined

surface with periodicity was desired for ease of manufacturing and modeling in computational studies. Of the different third-party software options available to design such a weave pattern, the open-source software TEXGEN was chosen based on the comparative analysis performed by Sherburn [19] and Nemeth et al. [20]. During their analysis, Nemeth, et al. determined that while the mesh generation capability of TEXGEN was inadequate, it does generate geometries that appropriately represent a weave.

For this study, the geometry chosen was a 5 Harness Satin (5HS) geometry based off of the weave originally described in Nemeth et al. [20]. The repetitive unit cell (RUC) for the geometry is made up of five upper and five lower tows, with each lower tow crossing over a single upper tow once per RUC. Within this pattern, each crossover point is spaced no less than two tow widths away from another crossover point [21]. One change made from the geometry used in Nemeth et al. [20] is the slight increase in fabric thickness to allow for better definition between tows at the crossover points. The resulting RUC has a tow width of 1.125 mm with a fabric thickness of 0.375 mm. Once the weave pattern was generated, the 3D weave geometry was filled on the bottom surface leaving a rectangle with the top surface in the shape of the CMC weave shown in Fig. 1. This completed surface RUC was then scaled 30 times larger, enabling a match to engine-relevant Reynolds numbers given the velocity range achievable in the tunnel. The resulting roughness values for the 30 $\times$  RUC are  $S_a = 1.14$  mm,  $S_q = 1.39$  mm, and  $S_z = 6.02$  mm. This large-scale unit cell was repeated five times in the streamwise direction to create the surface that was tested in this experiment.

## Experimental Methods

The experiments for this study were conducted within the recirculating wind tunnel first introduced by Eberly and Thole [22]. The height and width of the test section are 0.3 m  $\times$  0.3 m, respectively, and the tunnel can provide freestream velocities up to 17 m/s. The closed-loop construction of the tunnel means that the air temperatures can be controlled from ambient to 55  $^{\circ}$ C, using a chiller system and electric heaters. For this study, the air temperature was kept constant at  $\sim 20$   $^{\circ}$ C. Shown in Fig. 2 is the test section portion of the wind tunnel. A leading-edge suction loop was located just before the test surface to remove the incoming tunnel boundary layer and allow for a newly started boundary layer. A trip was located at the leading edge of the test plate to generate a turbulent boundary layer. Although it is likely the pattern of the CMC itself would result in a natural trip behavior, it was desirable to control the uniformity of the initial boundary layer development via the trip.

Given the weave pattern on the top surface, it was not straightforward to simply create a uniform heat flux on the surface. Instead, the

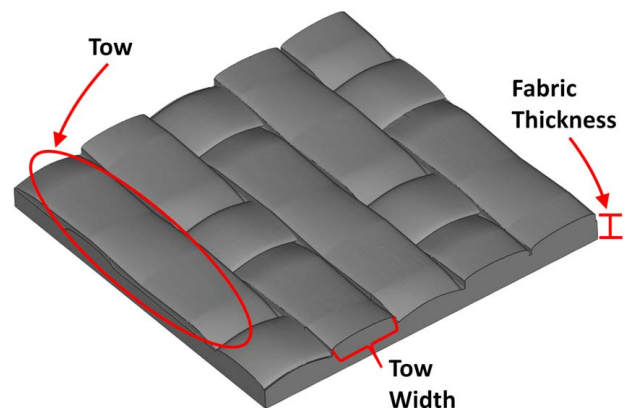


**Fig. 1** 5 Harness Satin repetitive unit cell for the CMC weave pattern

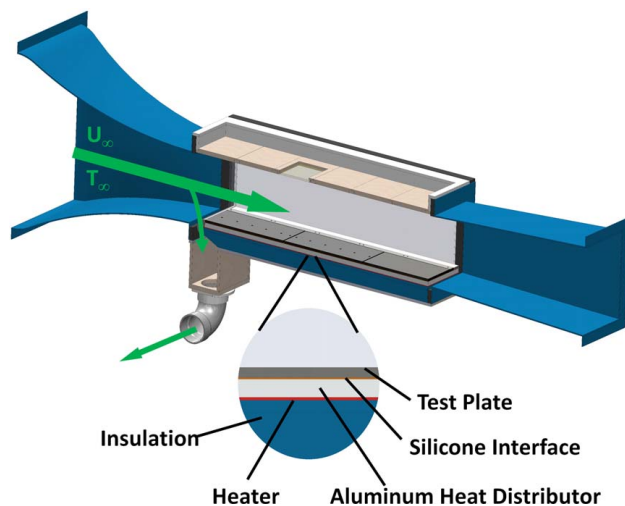


**Fig. 2** Cross section of the test section and expanded view of the five layers that compose the composite endwall

temperature difference across an insulating layer was imported into a finite element (FE) model, where the top temperature boundary condition (on the CMC surface) was obtained with an infrared (IR) camera, and the bottom boundary condition was a uniform temperature from a heated aluminum plate. The finite element model solution provides the local surface heat flux to calculate local heat transfer coefficients. This technique was also used by Gritsch et al. [23] for studies of heat transfer coefficients around film cooling holes. A newly designed composite endwall was constructed as shown in Fig. 2. The composite endwall is composed of five layers. The bottom layer is a foam layer that is 8 cm thick to minimize heat loss. The foam is pressed against three thin-film heaters that are attached to a single 2 cm thick aluminum plate, which provides a constant temperature boundary condition. The three heaters all span the width of the wind tunnel but have different streamwise lengths to help maintain a constant temperature on the top of the aluminum plate to within  $\pm 0.5^\circ\text{C}$ , by allowing each heater to be operated independently.

Above the aluminum sheet is a thin layer of silicone rubber that acts as an interface ensuring uniform thermal contact between the test plates on top of the silicone, and the aluminum sheet below. The top layer of the endwall assembly is composed of the CMC surface test plates. This layer consists of two 3D-printed plates that are 40 cm in length and 23 cm in width, as shown in Fig. 3. The two test plates were printed using a Photocentric Pro LCD printer with a layer height of  $50\ \mu\text{m}$  and a pixel density of  $137\ \mu\text{m}$  while using a high accuracy isotropic resin with a measured thermal conductivity of  $0.208\ \text{W}/(\text{m}\cdot\text{K})$ . The surface had to be printed in two plates due to the limited build volume of the printer. Since the plates are at  $30\times$  scale, the resolution of the printer is more than adequate to represent the finest details of the weave pattern, without artificial striations due to the printing process.

Two orientations of the CMC unit cell were studied. For the 0 deg test case shown in Fig. 3(a), spanwise oriented tows are marked “B,” and long streamwise oriented tows are marked “A,” which were a majority of the surface. Similarly, in Fig. 3(b), the 90 deg case is shown. The larger tows that make up the majority of the surface are oriented in the spanwise direction and designated by a “C,” while the smaller spanwise oriented tows are designated by a “D.”

At the interface joining the CMC test plates, a self-leveling silicone was used for most of the interface gap to ensure a reasonable thermal connection between the two plates. On top of the self-leveling silicone, a thin layer of high-temperature silicone was carefully shaped to match the surface profiles of the two plates. The screw holes in the center of the plate, necessary to firmly anchor

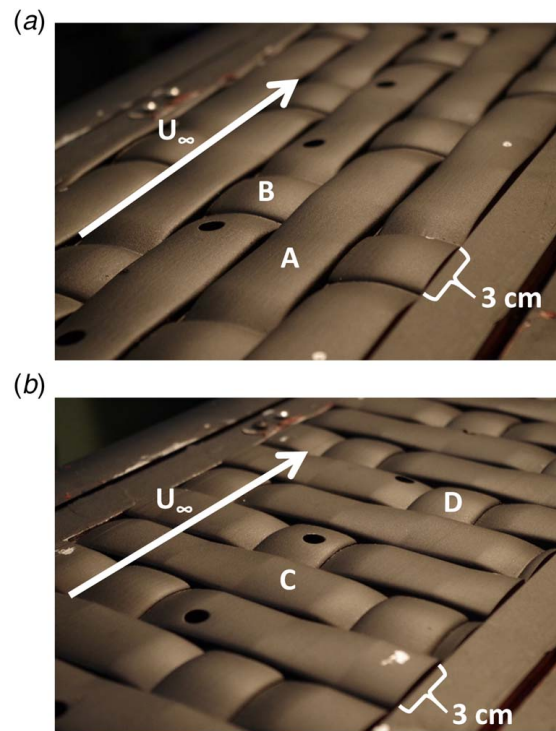


**Fig. 3** Images of (a) the 0 deg case with “A” and “B” designating the streamwise and spanwise oriented tows and (b) the 90 deg case with “C” and “D” designating the spanwise and streamwise oriented tows

the test plates to the aluminum (see Fig. 3), were filled in with putty and smoothed to be flush with the surrounding surface during testing so that they did not disturb the flow. Because they are locally a disturbance to the thermal boundary layer, however, the central region of the plate along the path of the screw holes was not included in the analysis of lateral average or area-averaged heat transfer.

On the top surface of the test plates, a thin layer of black Krylon paint was applied giving the surface an emissivity of 0.95 [24]. Aluminum bars on the lateral sides of the plate, used to secure the test plates to the endwall, also acted as temperature calibration sources for the infrared camera. To provide IR optical access across the entire length of the test plate, a series of six replaceable window elements were installed on the top endwall of the tunnel. This allowed for an element with a ZnSe IR transmissive window to be moved across the entire length of the plate.

Surface temperature measurements were taken using a FLIR T650SC infrared camera with an optical resolution of  $640\times 480$  pixels. Images were taken in sets of 10, with 10 s between each image, and then averaged together. This time-averaged image was calibrated using the thermocouple temperatures from the instrumented aluminum bars on either side of the test surface. Once calibrated, the images were transformed to the tunnel coordinate system using a projective transformation to account for the slight perspective distortion incurred by the angular orientation of the IR camera relative to the test plate. To cover the entire plate, the time-averaged images from four separate camera locations were stitched together using reference points that were printed into the plates to ensure accurate alignment.

**Heat Transfer Analysis Technique.** With measured surface temperatures generated by the IR images, the constant temperature provided by the aluminum heat spreader, and the material properties and geometry of the composite wall components, the steady surface heat flux for one-dimensional conduction  $q''_{\text{cond}}$  can be estimated



using Eq. (1). Because of the low thermal conductivity of the 3D-printed CMC surface plates, the heat transfer is largely one-dimensional. Calculating the heat flux through the plate using this one-dimensional assumption results in a local value for  $q''_{cond}$

$$q''_{cond}(x, z) = \frac{T_{Al} - T_s(x, z)}{\frac{t_{CMC}}{k_{CMC}} + \frac{t_i}{k_i}} \quad (1)$$

To fully account for three-dimensional conduction within the plastic layer representing the variable-thickness weave surface, however, a finite element model of the composite endwall was developed. This FE model was composed of the 3D-printed CMC plates and the silicone interface as shown in Fig. 4. The CMC geometry used in the FE model is the same as the model used to print the test plates allowing for an accurate representation of the surface geometry, while the silicone interface geometry is based on manufacturer specifications. A temperature boundary condition was imposed on the top surface of the CMC plate using the measured top surface temperatures from calibrated IR, and the constant wall temperature of the aluminum was imposed on the bottom of the silicone interface. The thermal conductivity and specific heat for the CMC test plate were obtained using a transient plane source technique [25], and the material properties from the silicone interface were obtained from manufacturer specifications. Note that the aluminum temperatures were measured using thermocouples and were uniform to within  $\pm 0.5$  °C. The local heat transfer coefficients were computed from the local surface heat flux obtained from the FE model

$$h(x, z) = \frac{q''_{cond}(x, z) - q''_{rad}(x, z)}{T_s(x, z) - T_\infty} \quad (2)$$

Note that the surface heat flux was corrected for radiation using the known emissivity of the surface and an average background temperature equal to the tunnel surrounding wall temperature. The resulting radiation heat flux was approximately 8% of the total surface heat flux. The local heat transfer coefficient was non-dimensionalized as a Stanton number using the measured free-stream velocity, air density, and air-specific heat capacity.

To ensure the complex surface features and 3D conduction in the CMC surface were fully resolved, a grid independence study was performed. From this study, calculations of local surface St using mesh sizes of 400,000 and 1,800,000 were different by only 0.5%

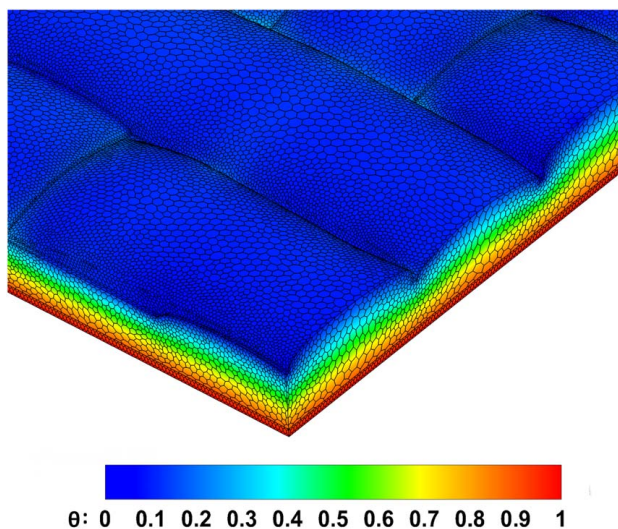


Fig. 4 Isometric view of the 90 deg 5HS test case showing non-dimensional temperature distribution across the test plate in addition to the mesh used for the analysis

and 0.4%, respectively, relative to the nominal 900,000 cell mesh used.

**Validation of Heat Transfer Analysis.** Because the method for measuring heat transfer coefficients was newly implemented for the facility, it was important to validate it. Local St numbers on a flat plate surface using the same plastic material were obtained using the technique previously described. Figure 5 shows spanwise-averaged heat transfer as a function of surface distance Reynolds number along the plate, compared with a turbulent flat plate correlation for constant surface temperature. Also included are the uncertainties in the measured St. Note that the plate top surface is not a constant temperature or a constant heat flux because of the nature of the conduction across the plastic, but for turbulent flow, the difference between the two boundary conditions is small. The missing data from  $4 \times 10^5 < Re_x < 5 \times 10^5$  results from this area containing the seam between the two plates. Good agreement was found between the measured spanwise-averaged St relative to the turbulent flat plate correlation.

**Boundary Layer Measurements.** Two-component boundary layer measurements were captured for the 0 deg and 90 deg orientation cases using a laser Doppler velocimeter (LDV). Green (532 nm) and yellow (561 nm) beam pairs were transmitted through a two-component transceiver probe with a focal distance of 350 mm and a half angle of 3.97 deg [26]. One of each laser pair was frequency-shifted by 40 MHz to prevent directional ambiguity in the flow measurements. In order to capture the near-wall flow without obstructing the beams, the probe head was angled 10 deg downward. This has a negligible impact on the vertical velocity component measurement because of the small angle. The elliptical measurement volume of the LDV beam crossing had an estimated length of 1.35 mm in the cross-stream (z) direction and an estimated diameter of 117  $\mu$ m in the wall-normal direction [27]. To collect the scattered light from the measurement volume, the LDV probe was operated in back-scatter mode. At each measurement point, 25,000 coincident samples were taken, except for the first few points very near the wall where the total number was reduced due to low sampling rates. Seeding particles of bis(2-ethylhexyl) sebacate (also known as DEHS) at approximately 1  $\mu$ m size were atomized and introduced upstream of the test section just prior to the fan, and were evenly distributed throughout the wind tunnel.

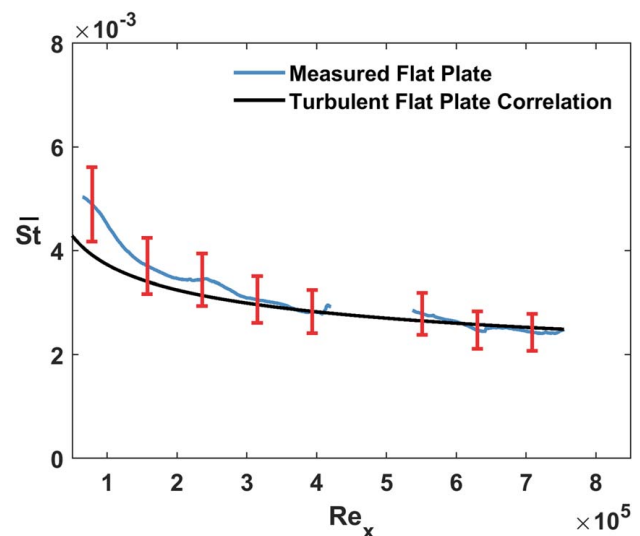


Fig. 5 Comparison between the measured St and the correlation for turbulent flow over a flat plate with a constant temperature boundary condition

**Uncertainty Analysis.** Uncertainty analyses were performed for both the boundary and heat transfer measurements. For the heat transfer analysis, the bias uncertainty was calculated using the partial differential method introduced in Moffat [28]. Using this method, the bias uncertainty was determined to be 11.6% for  $h$  and 14.1% for  $St$ . Bias uncertainty for the LDV system is 2% as indicated by the manufacturer. The precision uncertainties for both the heat transfer and the boundary layer measurements were calculated using the method described in Figliola and Beasley [29]. Using this method, at a confidence level of 95%, the precision uncertainty for  $h$  and  $St$  is 3.7%. Then, the overall uncertainty for  $h$  is 12.2% and is 14.6% for  $St$ . For the velocity measurements, precision uncertainty was determined to be 0.17% for the streamwise mean velocity, 3.7% for  $u'$ , and 1.3% for  $v'$ . Streamwise velocity has an overall uncertainty of 2%, while rms values are slightly higher with  $u'$  and  $v'$  having an overall uncertainty of 4.2% and 2.3%, respectively.

## Results and Discussion

Local  $St$  and boundary layer measurements were taken for the 5 Harness Satin weave unit cell, at two orientations relative to the flow as described earlier. For both cases, the range of  $Re$  numbers is relevant to the values found along a turbine airfoil surface [30].

**Effect of Weave Features on Local Heat Transfer.** The effects of weave orientation on the local, spanwise-averaged, and area-average  $St$  were evaluated for two weave orientations. Figure 6 shows the local  $St$  for the 0 deg and 90 deg cases as a function of  $Re_x$ . Note that the screw locations down the center of the plates are blanked, as they are invalid data, and the seam between the two separate plates is around  $Re_x = 4.4 \times 10^5$ . In general,  $St$  gradually decreases with increasing  $Re_x$  for both surfaces in Fig. 6, as would be expected from a growing thermal boundary layer. Also, the results indicate good lateral uniformity given the staggered offset patterns of the weave.

The local  $St$  variation, however, is more interesting. The 0 deg oriented weave in Fig. 6(a) has localized high levels of  $St$  in two general locations. The first is on the leading edges of the perpendicularly oriented (B) tows in a region where the flow is stagnating on the protruding surfaces. The second area of high local  $St$  is the leading edge of an A tow. Areas at the trailing edge of a protruding tow have slightly lower  $St$ , where the flow over the tow is likely separated. This pattern of lower  $St$  on the downstream face of a protruding tow and higher  $St$  on the leading edge of a protruding tow is generally consistent along the length of the plate.

Local  $St$  for the 90 deg case in Fig. 6(b) has many of the same trends as the 0 deg case, but shows more lateral uniformity due to

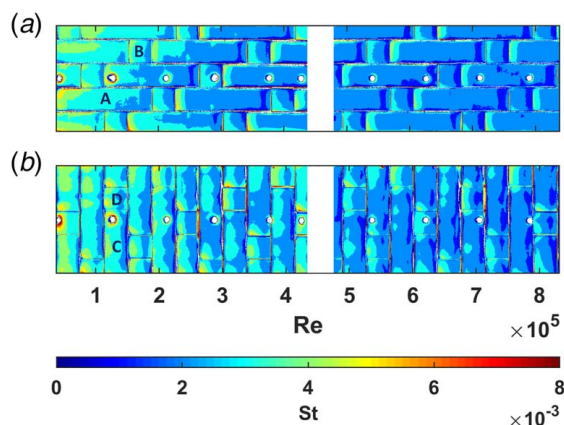


Fig. 6 Local  $St$  contours for the (a) 0 deg and (b) 90 deg 5HS weave orientations

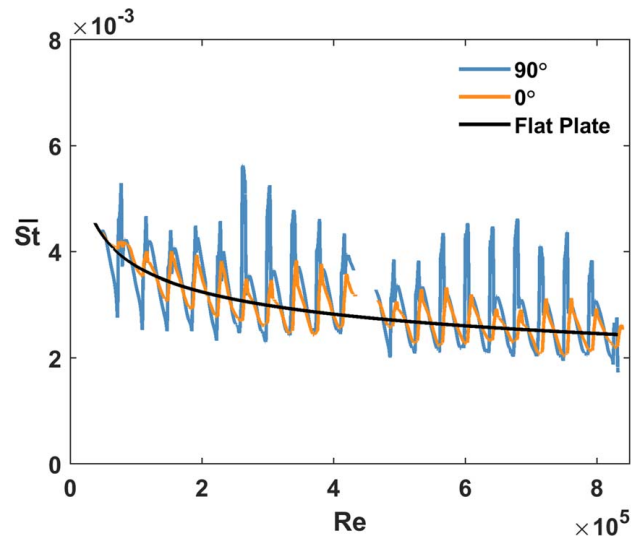


Fig. 7 Spanwise-averaged  $St$  of the 0 deg and 90 deg CMC surfaces over a smooth flat plate along with the  $St$  for a turbulent flat plate with a constant temperature boundary condition

the orientation of the long C tows. The area at the leading edge of a protruding tow demonstrates significantly higher  $St$ , and the downstream face of the tow has low  $St$ . Because of the cross-stream orientation of the C tows, high  $St$  values are present across a significant span of the plate, unlike the 0 deg case in Fig. 6(a) where high  $St$  regions are localized to the leading edge of the A tows. The CMC surface in a 90 deg orientation acts more like regular trips to the flow, which is known to enhance heat transfer.

Figure 7 shows the laterally averaged  $St$  as a function of the Reynolds number along the plate. A clear periodic pattern is present for both the 0 deg and 90 deg cases. This periodic pattern originates from the local changes in  $St$  as the boundary layer passes over surface weave features. Both orientations have a similar frequency between high and low  $St$ . The location of the peaks and troughs is directly related to the even tow widths that both surfaces were created from. The amplitude of this periodic pattern for the 0 deg case alternates above and below the turbulent flat plate correlation in roughly equal measure, indicating that the average  $St$  might be similar to a flat plate. The periodic pattern for the 90 deg orientation also alternates above and below the turbulent flat plate correlation; however, the peaks are biased toward high  $St$  indicating that average  $St$  will be higher than the flat plate.

$St$  augmentation contours in Fig. 8 were developed using the locally measured heat transfer normalized by the correlation for

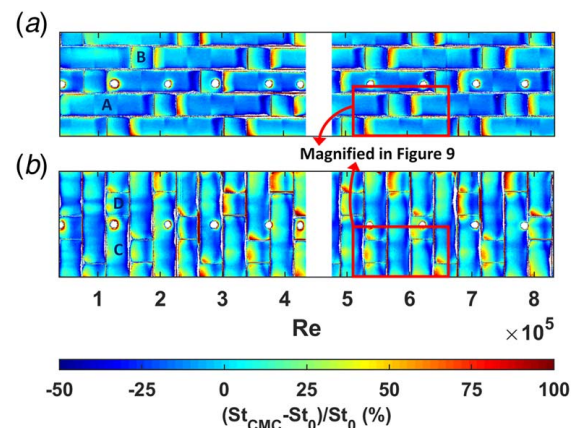


Fig. 8  $St$  augmentation of the (a) 0 deg and (b) 90 deg oriented CMC surfaces when compared with the  $St$  for a flat plate with a constant temperature boundary condition

turbulent flow on a flat plate with constant surface temperature. In this form, it is clearer how the local features around a tow impact the local heat transfer coefficient. The leading edge of a tow can exhibit augmentation values of over 100%, while there can be as much as a 50% reduction in the separated flow region at the trailing edge of a tow. After a  $Re_x$  of  $2 \times 10^5$  for the 0 deg plate, the local augmentation level at a given point on a tow is generally consistent with increasing downstream distance, indicating that the regular pattern of the CMC locally disturbs the boundary layer but the average trend follows the behavior of a turbulent flat plate. This also seems to be the case for the 90 deg orientation as well in Fig. 8.

Figure 9 shows a magnification of the area around  $Re_x = 5\text{--}6.5 \times 10^5$ , taken from Fig. 8. For the 0 deg case (Fig. 9(a)), tows that extend in the streamwise direction (A) for extended lengths have high augmentation values near their leading edge, but eventually result in augmentation that is near or equal to 0%. A region with local  $St$  below a turbulent flat plate is around the trailing edge of a streamwise tow (A), as it moves beneath a spanwise tow (B). These regions experience a substantial negative  $St$  augmentation approaching  $-50\%$ . Another area of negative  $St$  augmentation is on the downstream side of the spanwise tows (B) that cross the surface.

Augmentation of the 90 deg case as shown in Fig. 9(b) has a more widespread distribution of positive and negative  $St$  augmentation values.  $St$  augmentation in a region directly behind the transition from a spanwise tow (C) to a streamwise tow (D) has  $St$  augmentation ranging from 25% to 75% with some areas reaching augmentation values over 100%. The augmentation around the leading edge of a “D” tow also extends slightly to the sides, where the “C” tow underlaps the “D” tow. This complex region creates additional disturbance that locally augments  $St$ . The regions of negative  $St$  augmentation are present on the downstream side of a tow, where the surface slopes downward. These areas have augmentation values between  $-20\%$  and  $-40\%$ ; however, comparing to the 0 deg case in Fig. 9(a), the reduction in  $St$  (negative augmentation) in the downstream regions of a tow is not as significant.

Calculating the spanwise-averaged  $St$  augmentation for both the 0 deg and 90 deg cases as shown in Fig. 10 results in oscillating patterns that do not vary substantially with  $Re_x$ . The same trends described earlier are present in this plot: heat transfer is high at the leading edge of the tows and drops off along the tow, and the

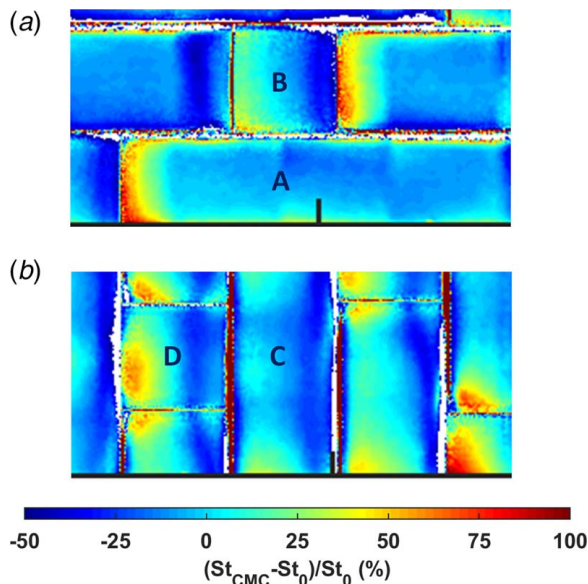


Fig. 9 Detailed view of  $St$  augmentation for (a) 0 deg and (b) 90 deg orientations from  $Re_x = 5\text{--}6.5 \times 10^5$  highlighting the change in  $St$  augmentation at tow crossover points and slight shape changes across the larger “A” and “C” tows

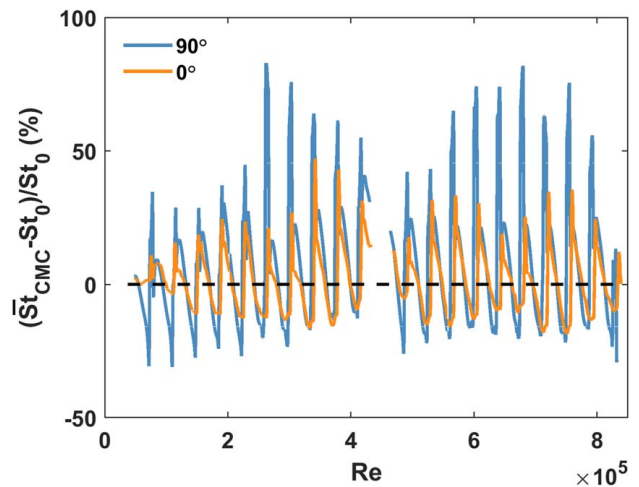


Fig. 10 Spanwise-averaged  $St$  augmentation of the 0 deg and 90 deg CMC surfaces when compared with the  $St$  for a flat plate with a constant temperature boundary condition

range and extent of augmentation is larger for the 90 deg case. On an area-average basis, the 0 deg case has an average augmentation of 0.8% relative to a turbulent flat plate. The 90 deg case has an overall  $St$  augmentation of 8.3%, due to the more extensive augmentation regions on the spanwise oriented (C) tows.

**Boundary Layer Measurements.** Four boundary layer profiles were taken for both the 0 deg and 90 deg test cases, to understand how the near-wall flow was affected by the CMC pattern. Figure 11(a) shows the locations for the 0 deg case, where locations 1 and 3 are near the leading edge of a B tow at the same relative position but at different  $Re_x$ , and locations 2 and 4 are near the trailing edge of the B tow and also at different  $Re_x$ . Likewise, Fig. 11(b) shows the four locations for the 90 deg case. These measurement locations were chosen to be near interesting regions of the surface heat transfer and are summarized in Table 1, but due to optical access challenges for measurements very close to the 3D surface, are not at the same physical location between the 0 deg and 90 deg oriented cases.

The normalized mean streamwise velocity profiles for the 0 deg case are shown in Fig. 12, where the wall-normal direction is normalized by the measured boundary layer thickness, and plotted in semi-log format to accentuate the near-wall region. The boundary

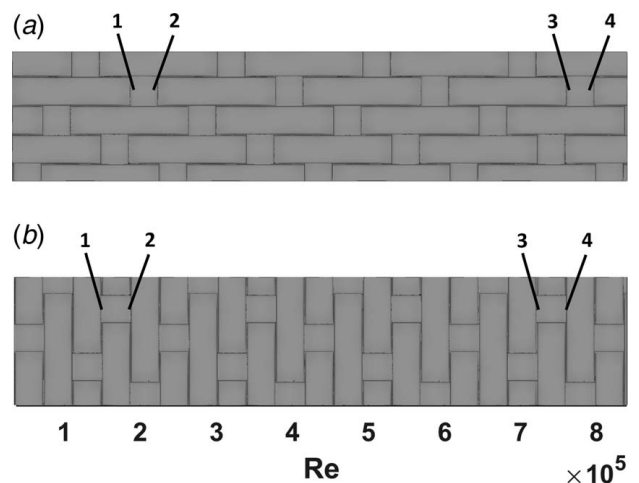


Fig. 11 The boundary layer measurement locations for the (a) 0 deg and (b) 90 deg oriented CMC surfaces



**Table 1 Summary of boundary layer measurements**

Case Location	0 deg orientation				90 deg orientation			
	1	2	3	4	1	2	3	4
Distance from leading edge ( $x/\lambda_{30}$ )	5.13	5.81	20.11	20.79	3.94	4.95	18.87	19.91
Distance from centerline ( $z/\lambda_{30}$ )	0.89	0.89	0.89	0.89	1.13	1.13	1.13	1.13
$U_\infty$ (m/s)	18.39	18.33	18.06	18.26	18.25	18.16	18.10	18.12
$Re_x$	$2.00 \times 10^5$	$2.26 \times 10^5$	$7.69 \times 10^5$	$8.04 \times 10^5$	$1.91 \times 10^5$	$1.91 \times 10^5$	$7.26 \times 10^5$	$7.66 \times 10^5$
$Re_\theta$	$5.20 \times 10^3$	$5.31 \times 10^3$	$5.35 \times 10^3$	$6.18 \times 10^3$	$6.34 \times 10^3$	$6.19 \times 10^3$	$9.41 \times 10^3$	$8.52 \times 10^3$
$\delta$ (mm)	21.79	22.63	29.23	32.56	13.59	15.54	34.04	34.33
$\delta^*/\delta$	0.20	0.20	0.16	0.16	0.39	0.34	0.24	0.21
$\theta/\delta$	0.14	0.13	0.12	0.11	0.13	0.14	0.10	0.11

layer thicknesses were determined by the height above the measurement surface where the velocity reached 99% of the freestream velocity. The 1/7th power law for an equilibrium flat plate turbulent boundary layer is also included for comparison. Note that the profiles are not plotted in inner coordinate form since wall shear stress was not directly measured. A study was performed to understand whether the Clauser chart method could be used to infer wall shear, or whether the total shear stress (mean velocity gradient plus turbulent stress) could be normalized with a guessed wall shear to produce a peak total stress value of one, but the results were not self-consistent for a given profile nor did they result in self-similar velocity profiles. This is not unexpected based on prior studies of turbulent boundary layers near or at separation and/or reattachment [31–33].

In Fig. 12, however, it does appear that locations 2 and 4 have laminar sublayer-like regions ( $Y/\delta < 0.05$ ), and logarithmic-like regions ( $0.1 < Y/\delta < 0.5$ ). At location 1 on the upstream side of a B tow, the velocity in the upper part of the boundary layer is low relative to a 1/7th power law, but is closer at the lowest points measured ( $Y/\delta < 0.02$ ). This suggests that the flow has a prior history of separated regions (with low momentum) that have migrated away from the wall, but is locally being accelerated near the wall below  $Y/\delta = 0.01$  due to the blockage of the front face of the tow. This is consistent with the high St found at the leading edge of B tows in Fig. 9(a). At location 2 in Fig. 11, on the downstream side of the B tow, the streamwise velocity below  $Y/\delta = 0.02$  drops dramatically. This indicates the separated flow region expected to exist here, based on the low St values in Fig. 9(a) found at the trailing edge of B tows.

The trend of locally accelerating near-wall flow at the front of a tow, versus low-speed separated flow at the downstream end of a tow, is generally similar for locations 3 and 4 in Fig. 12. Because

of the additional development of the boundary layer over the CMC surface at these downstream locations, the profiles have a logarithmic-like region that is closer to the 1/7th power-law behavior. The accelerated near-wall velocity is similar between locations 1 and 3, which might be why the augmentation at the leading edge of a B tow (Fig. 8(a)) is consistent along the length of the plate. However, the streamwise velocity throughout the boundary layer is slightly higher for location 4 versus location 2. The separated regions on the downstream end of a B tow may have a smaller size relative to the boundary layer at this high Reynolds number location along the plate.

The streamwise turbulence intensity (streamwise fluctuation RMS divided by freestream velocity) for the four measurement locations on the 0 deg oriented CMC is displayed in Fig. 13. In all profiles, the turbulence intensity is low in the freestream ( $Y/\delta > 1$ ) as expected for the wind tunnel. For location 1 on the leading edge of a B tow, streamwise turbulence intensity is relatively flat over the majority of the boundary layer, up to  $Y/\delta = 0.5$ . For the lowest measurable points below  $Y/\delta = 0.01$ , the trend does not seem to be going to zero, suggesting that fluctuations are high even close to the wall. For location 2 on the downstream side of the B tow, high levels of streamwise fluctuations are located at approximately the region of the steep drop in mean velocity indicated in Fig. 12. The unsteadiness in the flow is high in the recirculation zone that likely exists on the downstream side of the B tow.

The wall-normal turbulence intensity shown in Fig. 14 has an interesting behavior for locations 1 and 3, which are at the leading edge of a B tow. In both cases, the wall-normal fluctuations peak at about  $Y/\delta = 0.03$  and have a similar decay to zero below that level, but above that level are clearly different in the log-like region. Location 1 has higher wall-normal fluctuation levels than location 3 from  $Y/\delta = 0.1$  to 0.9, which is similar to the difference in

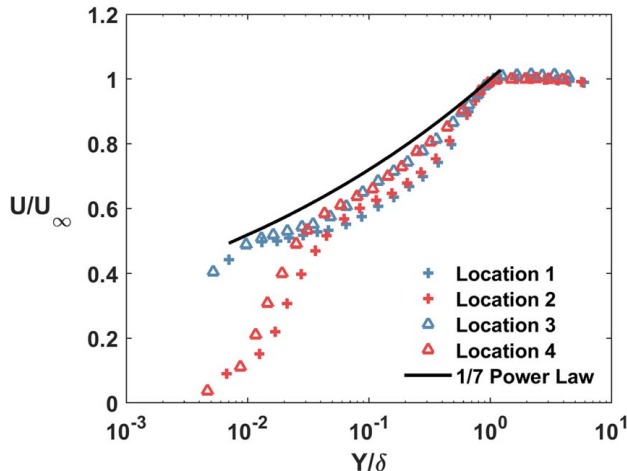


**Fig. 12 Streamwise velocity profiles for the 0 deg CMC surface**

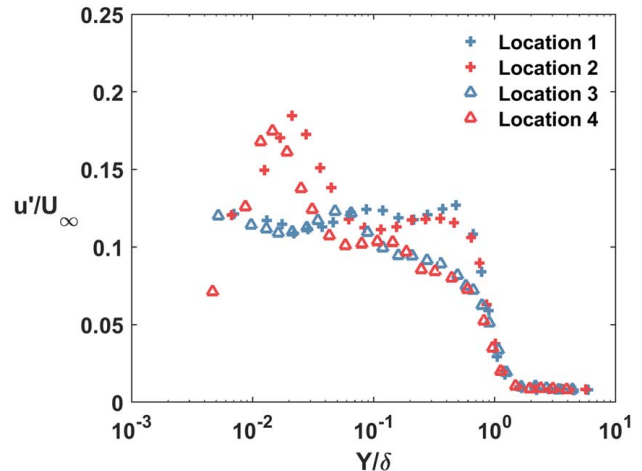


**Fig. 13 Turbulence intensity in the streamwise direction for the 0 deg CMC surface**

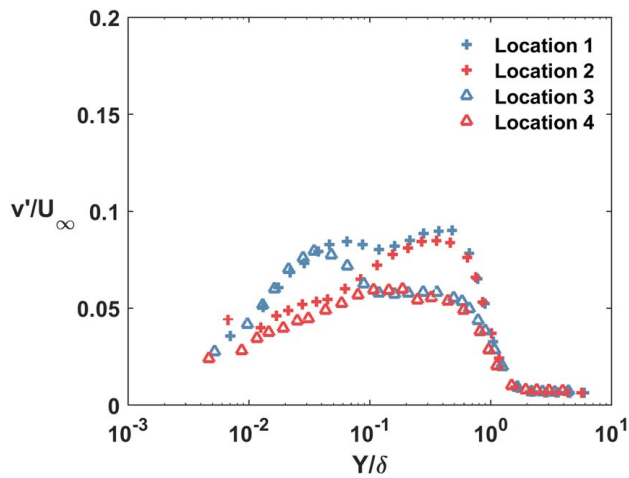


Fig. 14 Turbulence intensity in the wall-normal direction for the 0 deg CMC surface

streamwise fluctuation levels between location 1 and 3 in Fig. 14. This suggests large unsteadiness levels in the upper region of the early developing boundary layer on the CMC plate. The cause of these high fluctuation levels is not so clear without more detailed measurements but possibly is due to the convection of separated low-momentum zones into the upper boundary layer. Note also that  $\delta$  increases between locations 1 and 3, so peaks appear to be at a higher  $Y/\delta$  when  $\delta$  is small.

Figure 15 shows the streamwise mean velocity profiles for the 90 deg orientation case at the four measurement locations, compared with the 1/7th power law for a turbulent flat plate boundary layer. Note again from Fig. 11(b) that these measurements do not necessarily correspond to similar locations relative to the 0 deg plate in Fig. 11(a), due to the blockage of the LDV laser beams by the non-uniform surface very close to the wall. Although the streamwise velocity at location 4 somewhat resembles a turbulent boundary layer with laminar sublayer and logarithmic regions, clearly this orientation of the CMC dramatically disturbs the flow relative to smooth plate behavior. In fact, for all locations, there is slight negative streamwise velocity near the wall indicating recirculation is present. At location 1, below  $Y/\delta = 0.2$ , the steep drop in streamwise velocity indicates a large low-momentum zone which is probably the separated flow on the downstream face of a C tow. Location 2, located just before the leading edge of the next C tow, shows higher streamwise velocity than location 1 from  $0.03 < Y/\delta < 0.2$ . This is likely the reaccelerating flow caused by

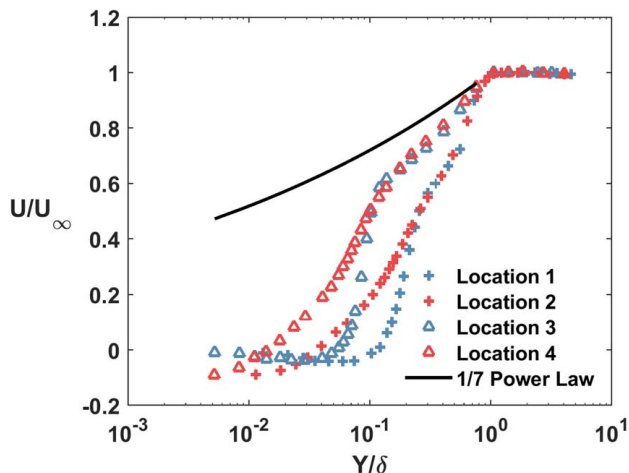


Fig. 15 Streamwise velocity profiles for the 90 deg CMC surface

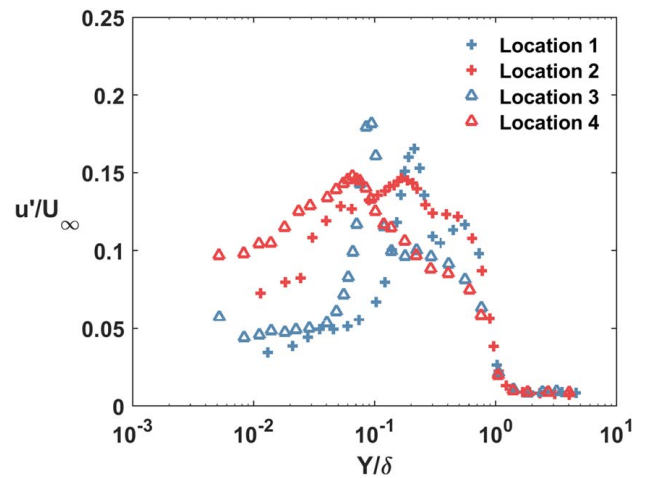


Fig. 16 Turbulence intensity in the streamwise direction for the 90 deg CMC surface

the blockage of the forward face of the C tow. From location 1 to location 3, the extent of the recirculation is decreasing in height relative to the local boundary layer thickness; that is, the transition from negative to positive  $U/U_\infty$  moves toward lower  $Y/\delta$ . A similar trend is seen between locations 2 and 4.

The streamwise turbulence intensity for the 90 deg CMC orientation is shown in Fig. 16. A narrow peak in turbulence intensity is seen at  $Y/\delta = 0.2$  for location 1, and  $Y/\delta = 0.1$  for location 3, which correspond to the  $y$ -locations in Fig. 15 where the streamwise mean velocity starts to rapidly decrease. This is indicative of an unsteady separated shear layer which likely contributes to the high heat transfer seen at this location in Fig. 9(b). At location 2, the peak turbulence intensity around  $Y/\delta = 0.2$  is reduced and broadened, but intensity levels below  $Y/\delta = 0.1$  are significantly higher than for location 1. At location 2, the near-wall flow is starting to undergo separation on the downstream face of the D tow. These behaviors of locations 1 and 2 are similar to locations 3 and 4 further along the CMC surface, except they move to lower  $Y/\delta$  since the features are smaller relative to the local boundary layer height. Wall-normal turbulence intensity displayed in Fig. 17 has similar trends to the streamwise turbulence intensity shown in Fig. 16. Narrow peaks in wall-normal fluctuations are present at  $Y/\delta = 0.2$  for location 1, which is the unsteady separated shear layer from the upstream tow. At location 2, the peak broadens, but increases in magnitude as the near-wall separated flow causes

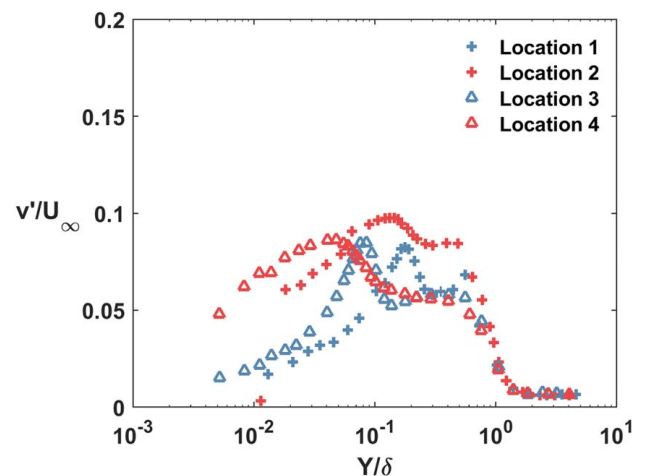
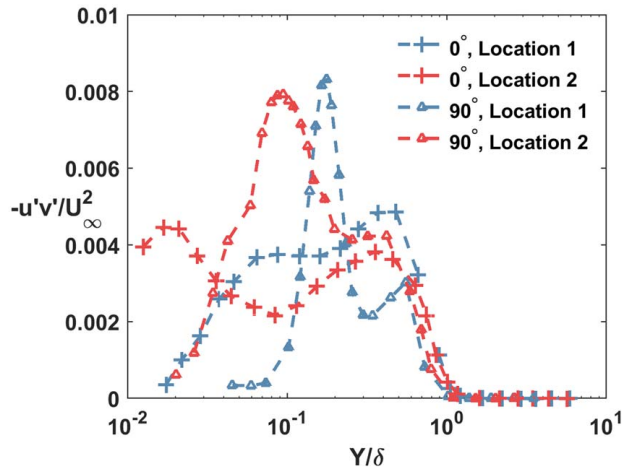


Fig. 17 Turbulence intensity in the wall-normal direction for the 90 deg CMC surface





**Fig. 18 Reynolds shear stress for the 0 deg and 90 deg CMC surfaces**

high vertical velocity fluctuations. Locations 3 and 4 further along the plate have similar peaks but at lower  $Y/\delta$ .

The normalized Reynolds shear stress for locations 1 and 2 on the 0 deg and 90 deg surfaces is shown in Fig. 18. Only the two locations are shown for each plate since the trends are similar for the other downstream locations. Also note that the profiles between 0 deg and 90 deg surfaces are not at exactly the same  $Re_x$ , but are close. For the 0 deg surface, the Reynolds stress at location 1 has a peak near the upper region of the boundary layer ( $Y/\delta = 0.4$ ), but at location 2, there are two peaks, with one very close to the wall near the separated region at the downstream edge of the tow. The 90 deg surface shows more dramatic peaks in Reynolds stress, with sharp peaks at  $Y/\delta$  heights corresponding to the location of flow reversal (negative streamwise velocity) indicated in Fig. 15 for locations 1 and 2. These peaks in Reynolds stress are associated with the unsteadiness of the upstream separated flow for the 90 deg surface.

## Summary and Conclusions

Local heat transfer coefficients and selected boundary layer measurements were obtained on a 5 Harness Satin weave surface representative of an uncoated CMC. The periodic weave pattern generates significant local augmentation relative to a flat plate, generally in regions where one tow transitions to another. In general, upstream facing surfaces have substantial St augmentation due to local flow acceleration, whereas backward-facing surfaces have negative St augmentation in the separated zones behind them; that is, the heat transfer can be reduced relative to a flat plate. Boundary layer measurements confirm that the flow is locally disturbed around the tow transitions and does not generally match a turbulent boundary layer behavior due to the regular disturbance of the weave pattern.

The orientation of the CMC weave pattern is clearly critical to the augmentation mechanisms. Orientations that position long tows perpendicular to the flow result in higher average St augmentation relative to an aligned orientation, since the tows act as flow trips. This behavior would be dependent on the weave pattern chosen, but it is recommended that the designer avoids patterns that would generate long tows perpendicular to the expected flow direction.

The significant local heat transfer augmentation seen in the geometrically perfect CMC plates in this study somewhat canceled out on an average basis particularly for the 0 deg orientation, resulting in minor increases in area-average heat transfer. However, the substantial positive and negative local heat transfer augmentation exemplifies the need for more sophisticated interrogation of the flow, and better roughness metrics to represent this effect.

## Acknowledgment

The authors would like to thank Pratt & Whitney for their generous support over the duration of this project.

## Conflict of Interest

There are no conflicts of interest.

## Data Availability Statement

The datasets generated and supporting the findings of this article are obtainable from the corresponding author upon reasonable request. The authors attest that all data for this study are included in the paper.

## Nomenclature

$h$	= heat transfer coefficient, $h = q''/(T_s - T_\infty)$
$k$	= thermal conductivity
$t$	= local thickness
$x$	= streamwise direction
$y$	= wall-normal direction
$z$	= spanwise direction
$T$	= temperature
$U$	= mean streamwise velocity
$k_s$	= equivalent sand grain roughness height
$q''_{cond}$	= heat flux from conduction
$q''_{rad}$	= heat flux from radiation
$u'$	= RMS of fluctuations in the streamwise velocity
$v'$	= RMS of fluctuations in the wall-normal velocity
$C_p$	= specific heat at constant pressure
$R_a$	= arithmetic mean height of a line
$S_a$	= arithmetic mean roughness
$S_q$	= root mean square roughness
$S_z$	= maximum roughness height
$T_{Al}$	= aluminum temperature
$T_s$	= plate surface temperature
$T_\infty$	= freestream temperature
$U_\infty$	= freestream velocity
$Pr$	= Prandtl number
$Re_x$	= Reynolds number $Re_x = U_\infty \times x/\nu$
$Re_\theta$	= momentum thickness Reynolds number, $Re_\theta = U_\infty \times \theta/\nu$
$St$	= Stanton number, $St = h/(\rho C_p U_\infty)$
$-u'v'$	= Reynolds shear stress

## Greek Symbols

$\delta$	= boundary layer thickness
$\delta^*$	= displacement thickness
$\theta$	= momentum thickness
$\theta$	= non-dimensional temperature, $\theta = (T - T_\infty)/(T_{Al} - T_\infty)$
$\lambda$	= tow width
$\lambda_{30}$	= tow width for 30x scaled geometry
$\rho$	= density
$\nu$	= kinematic viscosity

## Subscripts

<i>air</i>	= property of air
CMC	= property of CMC surface test plate
<i>cond</i>	= heat transfer from conduction
<i>i</i>	= property of silicone interface
<i>rad</i>	= heat transfer from radiation
0	= property of a flat plate

## References

- [1] Walock, M. J., Heng, V., Nieto, A., Ghoshal, A., Murugan, M., and Driemeyer, D., 2018, "Ceramic Matrix Composite Materials for Engine Exhaust Systems on Next-Generation Vertical Lift Vehicles," *ASME J. Eng. Gas Turbines Power*, **140**(10), p. 102101.
- [2] Padture, N. P., 2016, "Advanced Structural Ceramics in Aerospace Propulsion," *Nat. Mater.*, **15**(8), pp. 804–809.
- [3] Cinibulk, M. K., Apostolov, Z. D., Boakye, E. E., Key, T. S., and King, D. S., 2018, "Constituent Development for Higher-Temperature Capable Ceramic Matrix Composites," Proceedings of the ASME Turbo Expo, Oslo, Norway, June 11–15, Paper No. GT2018-76835.
- [4] Alvin, M., Anderson, I., Heidloffm, A., White, E., Bhatt, R., Grady, J., McMordie, B., and Warnes, B., 2015, "Development of Advanced Material Systems for Future Gas Turbine Applications," Proceedings of ASME Turbo Expo, Montréal, Canada, June 15–19, Paper No. GT2015-43456.
- [5] Presby, M. J., Nesredin, K., Sanchez, L. J., Faucett, D. C., Choi, S. R., and Morscher, G. N., 2019, "Life-Limiting Behavior of an Oxide/Oxide Ceramic Matrix Composite at Elevated Temperature Subject to Foreign Object Damage," *ASME J. Eng. Gas Turbines Power*, **141**(3), p. 031012.
- [6] Zhu, D., 2018, Aerospace Ceramic Materials: Thermal, Environmental Barrier Coatings and SiC/SiC Ceramic Matrix Composites for Turbine Engine Applications, NASA/TM—2018-219884.
- [7] Watanabe, F., Nakamura, T., and Mizokami, Y., 2017, "Design and Testing for Ceramic Matrix Composite Turbine Vane," Proceedings of ASME Turbo Expo, Charlotte, NC, June 26–30, Paper No. GT2017-63264.
- [8] Watanabe, F., Nakamura, T., and Shinohara, K. I., 2016, "The Application of Ceramic Matrix Composite to Low Pressure Turbine Blade," Proceedings of the ASME Turbo Expo, Seoul, South Korea, June 13–17, Paper No. GT2016-56614.
- [9] Bogard, D. G., Schmidt, D. L., and Tabbita, M., 1998, "Characterization and Laboratory Simulation of Turbine Airfoil Surface Roughness and Associated Heat Transfer," *ASME J. Turbomach.*, **120**(2), pp. 337–342.
- [10] Bons, J. P., 2010, "A Review of Surface Roughness Effects in Gas Turbines," *ASME J. Turbomach.*, **132**(2), p. 021004.
- [11] Bons, J. P., and McClain, S. T., 2004, "The Effect of Real Turbine Roughness With Pressure Gradient on Heat Transfer," *ASME J. Turbomach.*, **126**(3), pp. 385–394.
- [12] Buckles, J., Hanratty, T. J., and Adrian, R. J., 1984, "Turbulent Flow Over Large-Amplitude Wavy Surfaces," *J. Fluid Mech.*, **140**, pp. 27–44.
- [13] Mamori, H., Fujimura, M., Udagawa, S., Iwamoto, K., Murata, A., Kaqaguchi, Y., Ando, H., Kawashima, H., and Mieno, H., 2018, "Effect of Wavelength of Sinusoidal Wavy Wall Surface on Drag and Heat Transfer at Turbulent Thermal Boundary Layer Flow," *J. Therm. Sci. Technol.*, **13**(2), pp. 1–11.
- [14] Busse, A., Thakkar, M., and Sandham, N. D., 2017, "Reynolds-Number Dependence of the Near-Wall Flow Over Irregular Rough Surfaces," *J. Fluid Mech.*, **810**, pp. 196–224.
- [15] Prokein, D., von Wolfersdorf, J., Dittert, C., and Böhrk, H., 2018, "Transpiration Cooling Experiments on a CMC Wall Segment in a Supersonic Hot Gas Channel," International Energy Conversion Engineering Conference, Cincinnati, OH, July 9–11, Paper No. AIAA 2018-4696.
- [16] Zhong, F., and Brown, G. L., 2009, "Experimental Study of Multi-Hole Cooling for Integrally-Woven, Ceramic Matrix Composite Walls for Gas Turbine Applications," *Int. J. Heat Mass Transfer*, **52**(3–4), pp. 971–985.
- [17] Krishna, K., Ricklick, M. A., Poinsatte, P., and Thurman, D., 2016, "Preliminary Investigation of an Oblique Jet Impingement Cooling on CMC Rough Surface," 52nd AIAA/SAE/ASEE Joint Propulsion Conference, Salt Lake City, UT, July 25–27, Paper No. AIAA 2016-4851.
- [18] Krishna, K., and Ricklick, M., 2017, "Heat Transfer Analysis of Jet Impingement Cooling on a Simulated Ceramic Matrix Composite Surface," Proceedings of the ASME Turbo Expo, Charlotte, NC, June 26–30, Paper No. GT2017-64991.
- [19] Sherburn, M., 2007, "Geometric and Mechanical Modelling of Textiles," Ph.D. dissertation, University of Nottingham.
- [20] Nemeth, N. N., Mital, S. K., and Lang, J., 2010, Evaluation of Solid Modeling Software for Finite Element Analysis of Woven Ceramic Matrix Composites, NASA/TM—2010-216250.
- [21] Barbero, E. J., 2010, *Introduction to Composite Materials Design*, CRC Press LLC, Boca Raton, FL.
- [22] Eberly, M. K., and Thole, K. A., 2014, "Time-Resolved Film-Cooling Flows at High and Low Density Ratios," *ASME J. Turbomach.*, **136**(6), p. 061003.
- [23] Gritsch, M., Schulz, A., and Wittig, S., 2000, "Film-Cooling Holes With Expanded Exits: Near-Hole Heat Transfer Coefficients," *Int. J. Heat Fluid Flow*, **21**(2), pp. 146–155.
- [24] Wittig, S., Schulz, A., Gritsch, M., and Thole, K. A., 1996, "Transonic Film-Cooling Investigations: Effects of Hole Shapes and Orientations," Proceedings of the ASME Turbo Expo, Birmingham, UK, June 10–13, Paper No. 96-GT-222.
- [25] 2015, "Hot Disk Thermal Constants Analyser Instruction Manual," Hot Disk AB, Gothenburg, Sweden.
- [26] 1994, "Model 9800 Series Fiberoptic Probes," TSI Incorporated, Shoreview, MN.
- [27] 2017, "Phase Doppler Particle Analyzer (PDPA)/Laser Doppler Velocimeter (LDV)," TSI Incorporated, Shoreview, MN.
- [28] Moffat, R. J., 1982, "Contributions to the Theory of Single-Sample Uncertainty Analysis," *J. Fluids Eng. Trans. ASME*, **104**(2), pp. 250–258.
- [29] Figliola, R. S., and Beasley, D. E., 2011, *Theory and Design for Mechanical Measurements*, John Wiley & Sons, Inc, Hoboken, NJ.
- [30] Colban, W., Gratton, A., Thole, K. A., and Haendler, M., 2006, "Heat Transfer and Film-Cooling Measurements on a Stator Vane With Fan-Shaped Cooling Holes," *ASME J. Turbomach.*, **128**(1), pp. 53–61.
- [31] Skote, M., and Henningson, D. S., 2002, "Direct Numerical Simulation of a Separated Turbulent Boundary Layer," *J. Fluid Mech.*, **471**, pp. 107–136.
- [32] Coleman, G. N., Rumsey, C. L., and Spalart, P. R., 2018, "Numerical Study of Turbulent Separation Bubbles With Varying Pressure Gradient and Reynolds Number," *J. Fluid Mech.*, **847**, pp. 28–70.
- [33] Kitsios, V., Sekimoto, A., Atkinson, C., Sillero, J. A., Borrell, G., Gungor, A. G., Jiménez, J., and Soria, J., 2017, "Direct Numerical Simulation of a Self-Similar Adverse Pressure Gradient Turbulent Boundary Layer at the Verge of Separation," *J. Fluid Mech.*, **829**, pp. 392–419.